ACS central science

http://pubs.acs.org/journal/acscii

Research Article

Visible Light Chemical Micropatterning Using a Digital Light Processing Fluorescence Microscope

Uroob Haris, Joshua T. Plank, Bo Li, Zachariah A. Page, and Alexander R. Lippert*

Cite This: *ACS Cent. Sci.* 2022, 8, 67−76

Read Online

ACCESS | Metrics & More | Article Recommendations | Supporting Information

ABSTRACT: Patterning chemical reactivity with a high spatiotemporal resolution and chemical versatility is critically important for advancing revolutionary emergent technologies, including nanorobotics, bioprinting, and photopharmacology. Current methods are complex and costly, necessitating novel techniques that are easy to use and compatible with a wide range of chemical functionalities. This study reports the development of a digital light processing (DLP) fluorescence microscope that enables the structuring of visible light (465−625 nm) for high-resolution photochemical patterning and simultaneous fluorescence imaging of patterned samples. A range of visible-light-driven photochemical systems, including thiol−ene photoclick reactions, Wolff rearrangements of diazoketones, and photopolymerizations, are shown to be compatible with this system. Patterning the chemical functionality onto microscopic polymer beads and films is accomplished with photographic quality and resolutions as high as 2.1 μm for Wolff rearrangement chemistry and 5 μm for thiol−ene chemistry. Photoactivation of molecules in living cells is demonstrated with single-cell resolution, and microscale 3D printing is achieved using a polymer resin with a 20 μm *xy*-resolution and a 100 μm *z*-resolution. Altogether, this work debuts a powerful and easy-to-use platform that will facilitate next-generation nanorobotic, 3D printing, and metamaterial technologies.

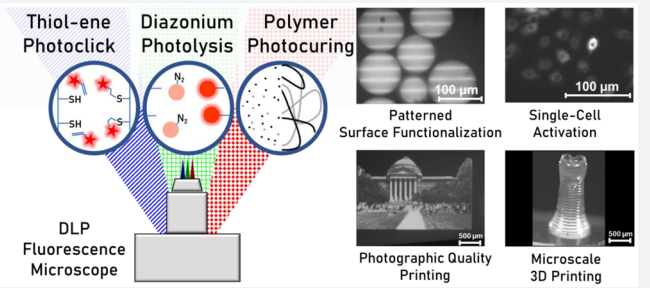

INTRODUCTION

Controlling the assembly of materials and chemical reactions with high spatial and temporal precision is critical to advances in established industries (integrated circuits, photovoltaics, displays, biotechnology, etc.)[1] and in emerging industries such as nanorobotics,[2] bioprinting,[3] microfluidics and analytical chemistry,[4] photopharmacology,[5,6] and additive manufacturing.[7] High-resolution nanofabrication methods such as electron-beam lithography,[8] focused ion-beam lithography,[9] scanning probe dip-pen nanolithography,[10] direct laser writing or multiphoton fabrication,[2] and nanoimprint lithography[11] can achieve high resolutions but are low-throughput and have high costs and limited chemical versatility. On the other hand, optical methods such as laser-based stereolithography, laser-induced forward transfer, selective laser sintering, and digital light processing (DLP) are relatively inexpensive and high-throughput and offer access to diverse light-mediated chemistries.[2,12] Rare (but potentially transformative) examples of chemically versatile nanofabrication have enabled the production of advanced multifunctional materials, including a 3D-printed sea cucumber mimic,[13] gecko-inspired adhesives,[14] cloaking devices,[15] and other complex metamaterials.[16]

DLP methods, which use digital micromirror devices (DMD) that can independently address each pixel and thereby structure light,[17] offer the advantages of high fabrication speeds, scalability, and high resolution.[2] These methods are often referred to as projection microstereolithography (PμSL)[18] or microscale continuous optical printing (μCOP)[19] and typically use UV light (364−405 nm) to induce polymerization with micrometer-scale resolutions. Notable advances include the use of a 200× objective[20] and microlens or pinhole arrays.[21] These types of systems have been applied for 3D printing plastics[22] and dynamic covalent materials[23] and in a combined microscopy system for the real-time polymerization of *Caenorhabditis elegans* assays,[24] with resolutions between approximately 1 and 25 μm. UV light, however, limits the scope of compatible materials, increases the cost of optics, and can interfere with certain chemistries. For these reasons, blue light (450−485 nm) DLP systems are beginning to be explored for hydrogels and bioprinting.[25,26] Despite these promising advances, microprinting using lower-energy green or red light remains rare, particularly with DLP systems that have largely been limited to use with polymerization chemistry. Moreover, integrating DLP with fluorescence microscopy is underexplored.

Received: October 7, 2021
Published: December 20, 2021

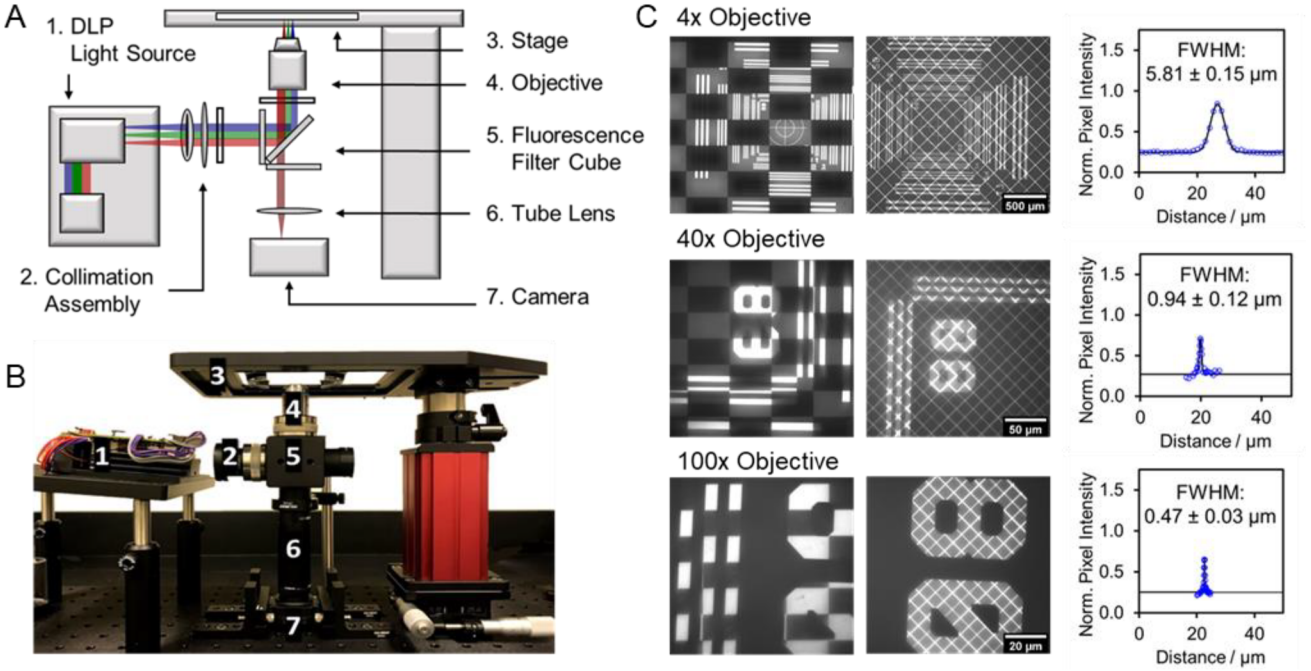

Figure 1. (A) Design scheme and (B) photograph of the DLP microscope setup composed of (1) a DLP LightCrafter 4500 as the patterned light source; (2) a light collimation assembly consisting of an adjustable iris diaphragm and an achromatic doublet collimation lens with a 100 mm focal length mounted in a zoom housing with 4.1 mm linear travel; (3) an *xy*-translational stage and slide holder; (4) a 4× objective (NA = 0.10), a 40× objective (NA = 0.60), or a 100× oil objective (NA = 1.30) mounted in a zoom housing with 4.1 mm linear travel; (5) a fluorescence imaging filter cube containing a 650 nm short-pass excitation filter, a 660 nm dichroic beamsplitter, and a 692/40 nm bandpass emission filter; (6) a mounted 100 mm focal length achromatic doublet lens in a 2.5" lens tube and a 1.0" spacer; and (7) a Chameleon3Monochrome sCMOS camera. Part details are provided in Table S1. (C) Checkerboard pattern and one-pixel-width diagonal lines projected onto a target resolution slide using 4×, 40×, and 100× objectives. The projection resolution with each objective was determined as the fwhm of the Gaussian fit (black line) to imaged pixel intensities (blue circles) across projected one-pixel-wide lines. The error on the fwhm is ±SD with n = 3 different lines measured.

Advancements in photoclick and photopolymerization chemistries make them ideally poised for integration with micropatterning.[12,27] One attractive photochemical system for micropatterning is thiol−ene photoligation.[28,29] Visible-light thiol−ene reactions can be conducted with eosin y as a photoinitiator,[30] and this chemistry has been used in a versatile molecular patterning technique employing multiphoton rasterization.[31,32] The photochemistry of diazoacetates and diazonium-photocaged compounds has also been exploited, particularly for photoactivatable single-molecule localization experiments[33,34] and photochemical synthetic transformations,[35] but there are very limited examples of photochemical patterning with this motif.[36] Recently, photopolymerization resins for visible-light 3D-printing have also been developed for use with DLP technology and multicolor photoinitiation, and efforts to improve the printing resolution with these are ongoing.[37,38]

Here, we report the development of a DLP fluorescence microscope and the associated photochemistry capable of performing photochemical reactions using blue (465 nm), green (520 nm), and red (624 nm) light with high spatiotemporal precision. Molecular micropatterning of silicon rhodamine dyes onto solid polymer beads was carried out and tracked using the built-in fluorescence microscope, and high-resolution 2D and 3D polymerizations were achieved using recently disclosed visible-light formulations.[37] Using a photoactivatable diazoketone-caged rhodamine dye, we demonstrate that this apparatus and chemistry can be used to perform spatial patterning of molecules inside living cells with single-cell resolution as well as to print fluorescence images onto polymer films with photographic quality and a resolution as high as 2.1 μm.

RESULTS AND DISCUSSION

DLP Microscope Design and Fabrication. To achieve highly resolved and spatially precise chemistry, we designed and constructed a digital light processing (DLP) fluorescence microscope capable of projecting patterned visible light onto micrometer-scale substrates with simultaneous fluorescence imaging (Figure 1A and B). Digital light processing was accomplished using the digital micromirror device and projection engine in a LightCrafter 4500 projector (Texas Instruments). Previously, we employed the LightCrafter and similar projectors in the fabrication of a volumetric 3D digital light photoactivatable dye display (3D Light PAD) for the patterned activation and excitation of photoswitchable fluorophores with ultraviolet and visible light.[39,40] For the DLP microscope, the LightCrafter was used with its projection optics removed. The setup includes a DLP4500FQE DMD chip and an IPD 1231 light engine containing collimated red, green, and blue LEDs.[17] Light from the LEDs is projected toward the DMD chip, and the reflected light from the DMD mirrors is directed through an adjustable diaphragm aperture, followed by collimation using a 100 mm achromatic doublet collimation lens. The collimated patterned light is then directed through a dichroic mirror to reflect short-wavelength excitation light and transmit long-wavelength light, and an emission bandpass filter is used to transmit light from 672−712 or 583−603 nm, regions that correspond with the

https://doi.org/10.1021/acscentsci.1c01234
ACS Cent. Sci. 2022, 8, 67−76

fluorescence emission of the red fluorescent dyes used in this study. For nonfluorescent samples, the filter cube could be easily replaced with one fitted with a 90:10 optical beamsplitter for reflected light microscopy. A 4× objective (NA = 0.10), a 40× objective (NA = 0.60), and a 100× objective (oil, NA = 1.30) were used to focus light onto a sample slide that could be moved using an *xy*-translational stage. Fluorescence emission from the sample was collimated through the objective and directed back through the filter cube, then focused through a tube lens (100 mm achromatic doublet) onto the sensor of a Chameleon3Monochrome sCMOS camera. A photograph of the DLP microscope is shown in Figure 1B, and vendors and part numbers are included in the SI (Table S1). Two zoom housings were included. The first was between the filter cube and the collimation lens to allow for fine control of the collimation of the patterned light from the DLP chip. It is important that this light is collimated when it enters the back aperture of the objective so that the patterned light is focused onto the imaging focal plane. Another zoom housing was inserted between the filter cube and objective to enable the sample to be focused on for imaging. Once the projected light is focused with the first zoom housing, it will match the imaging focus thereafter. The modular design of the DLP microscope also enabled the easy incorporation of supplemental elements; with the addition of a single-axis motorized translational stage to the existing setup, a 3D printing-capable microscope was achieved as described below.

DLP Microscope Characterization. Following the construction of the DLP microscope, we evaluated the light patterning capability of the system using the checkerboard, horizontal lines, and diagonal lines internal test patterns of the LightCrafter 4500 (Figures 1C and S1). Patterned light was projected through a 90:10 beamsplitter onto a microscope resolution target slide (Thorlabs, no. R1L3S10P) using the red LED and 4×, 40×, and 100× objectives. With each objective, sharp patterns were achieved with good light−dark contrast that could be tuned using the adjustable diaphragm aperture (Figure S1). The resolution of the projection was evaluated using the single-pixel-width diagonal lines internal test pattern. An intensity profile across the projected diagonal lines was generated in ImageJ (Figure 1C), and the resolution was determined as the full-width at half-maximum (fwhm) of the resultant Gaussian profiles. Using this method, we determined the projection resolutions were 5.81 ± 0.15 μm with the 4× objective, 0.94 ± 0.12 μm with the 40× objective, and 0.47 ± 0.03 μm with the 100× objective. The irradiation capability of the DLP microscope was also characterized (Figure S2 and Table S2). Using a Si photodiode sensor and a digital optical power meter (ThorLabs, nos. S120VC and PM100D, respectively), we measured the power density during irradiation with each LED of the LightCrafter using the different objectives and varying the LED current settings. The maximum power densities achieved with the 4× objective were 0.22 ± 0.02 W cm^{-2} with the red LED, 0.30 ± 0.04 W cm^{-2} with the green LED, and 0.48 ± 0.07 W cm^{-2} with the blue LED. With the 40× objective, the maximum power densities achieved were 7.17 ± 0.35, 10.33 ± 1.02, and 17.93 ± 1.53 W cm^{-2} for the red, green, and blue LEDs, respectively. Owing to the short focal length and working distance of the 100× objective, power density measurements under this objective using the standard photodiode sensor could not be obtained.

Visible-Light-Based Reaction Systems. We next turned our attention to photoinitiated chemical reactions that we could employ for chemical microprinting using the DLP microscope. We investigated the thiol−ene photoclick reaction between thiols and alkenes, which can be initiated by a visible-light photoinitiator, and the light-mediated insertion of diazo compounds into nucleophilic functionalities such as O−H and N−H bonds via direct carbene insertion or ketene trapping of their Wolff rearrangement products (Scheme 1). These

Scheme 1. Light-Based Thiol−Ene Photoclicking and Wolff Rearrangement of Diazoketones

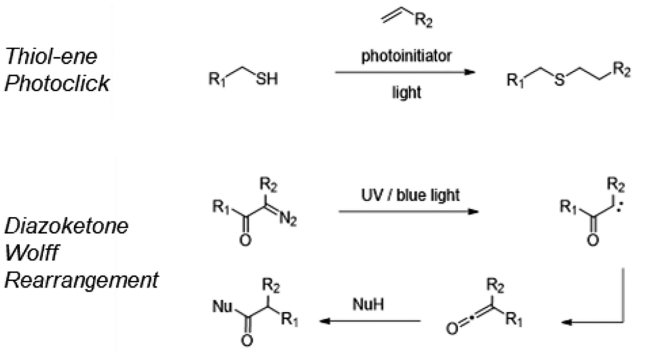

chemistries interested us because of their fast kinetics and high yields in response to visible light (Figure S3), so we leveraged them for observable covalent modification of thiol-, amine-, or alcohol-containing polymer constructs with fluorescent rhodamine molecules. We immobilized free thiols on commercially available NovaSyn-TG amino beads, which are made of 90 μm diameter polymer spheres commonly used in peptide synthesis; amide coupling with fmoc- and mmt-protected cysteine and subsequent cleavage of the mmt group with 1% trifluoroacetic acid (TFA) yielded the thiol-modified SH−resin as a platform for thiol−ene chemistry (Figure 2A). Next, we prepared the fluorescent alkene reaction partner silicon rhodamine−styrene (**SiR−sty**), which was designed to result in increased fluorescence at the sites of thiol−ene ligation on the SH−resin beads. The known precursor **SiR** was synthesized from the silicon anthrone **1** and *tert*-butyl-protected 3-iodo-4-methylbenzoic acid using *n*-butyllithium following a previously published protocol,[41] and a standard amide coupling of **SiR** with 4-amino styrene provided the thiol−ene partner **SiR−sty** in a high yield (Figure 2B). The value of λ_{max} for **SiR−sty** was found to be 685 nm in DMSO (Figure S4). We reacted the thiol-modified SH−resin with **SiR−sty** and eosin y in DMSO under blue light irradiation for 22 h and observed strong fluorescence emission from the beads when the reaction was irradiated as compared to almost no emission being observed when the reaction was conducted in the dark, confirming that on-bead reaction progress could be monitored via the fluorescence emission of **SiR−sty** (Figure 2C). Ellman's reagent was used to further verify that irradiation with blue light led to the depletion of free thiols and that the reaction with **SiR−sty** resulted in a 79 ± 13% conversion (Figure S5 and Table S3).

For photochemical patterning with diazo compounds, we envisioned the use of a fluorescent turn-on approach employing the Wolff rearrangement of the rhodamine B-based diazonium photocaged dye rhodamine BNN (**RhBNN**).[33] Upon the photolysis of **RhBNN**'s diazoketone caging group with blue light, a carbene is generated, which rapidly undergoes a Wolff rearrangement to a ketene

https://doi.org/10.1021/acscentsci.1c01234
ACS Cent. Sci. 2022, 8, 67−76

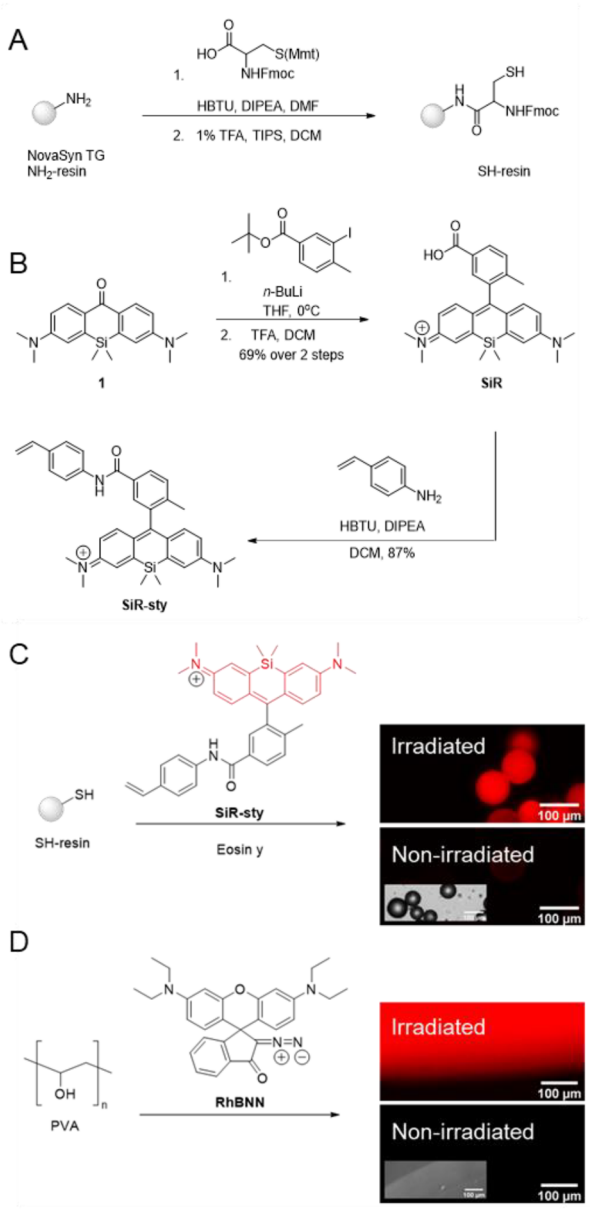

Figure 2. Visible-light-mediated reaction systems for solid microprinting. (A) Synthesis of the thiol-functionalized SH−resin. (B) Synthesis of the fluorophore-tagged alkene, **SiR−sty**. (C) Reaction scheme and EVOS-*fl* fluorescence images (Ex = 635/18 nm and Em= 692/40 nm) of washed SH−resin beads after being reacted in a solution of 3 mM **SiR−sty** and 70 μM eosin y in DMSO for 22 h with and without blue light irradiation from a 100 W LED lamp at 0.04 W cm^{-2}. (D) Reaction scheme and EVOS-*fl* fluorescence images (Ex = 542/20 nm and Em = 593/40 nm) of PVA films doped with 20 μM **RhBNN** with and without 22 h blue light irradiation from a 100 W LED lamp at 0.04 W cm^{-2}. The insets show brightfield images.

intermediate. The ketene can be subsequently trapped by nucleophilic species such as alcohols and amines to uncage the bright fluorescence emission characteristic of rhodamine B (Figure S4). Though we found that the Wolff rearrangement products of **RhBNN** undergo photobluing with long exposure to high-intensity light similar to other similar organic fluorophores,[42] the relatively short irradiation durations and low light intensities in our studies did not cause photobluing (Figure S4E−H). We used poly(vinyl alcohol) (PVA) to prepare films doped with **RhBNN**, theorizing that the solid PVA could also serve as the source of the nucleophilic hydroxyl groups required to trap the uncaged **RhBNN**. This was confirmed when we irradiated 50 μm thick films of PVA containing rhodamine BNN (**RhBNN**−PVA), which was coated onto glass microscope slides, with blue light; the films irradiated with blue light for 22 h displayed stronger red fluorescence as compared to those that were kept in the dark (Figure 2D).

Optimization of Procedures for Chemical Micropatterning. Next, we proceeded to apply this chemistry for surface micropatterning using the newly developed DLP microscope for patterned visible-light irradiation and fluorescence imaging. We first attempted micropatterning using a 4× objective. SH−resin beads were added onto a glass microscope slide with 20 μL of a **SiR−sty** and eosin y solution in DMSO. Patterned light in a grid pattern from the LightCrafter system was focused onto a field of the beads through the fluorescence filter cube and a 4× objective (Figure 3A). After 15 min of patterned illumination with high-intensity blue light (0.5 W cm^{-2}), the red fluorescence emission of the sample was imaged using a uniform field of weak excitation light (0.02 W cm^{-2}) through the the filter cube was optimized for silicon rhodamine fluorescence. Clear patterns were observed on the beads, indicating the successful 3D microprinting of a silicon rhodamine dye on the solid bead surface (Figure 3B). The covalent attachment of the dye was further confirmed by washing the beads thoroughly with DMSO and imaging them on an EVOS-*fl* fluorescence microscope through an Invitrogen Cy5-optimized filter cube (Ex = 635/18 nm and Em = 692/40 nm, ThermoFisher, no. AMEP4956) (Figure 3C). Micropatterning experiments with **RhBNN**−PVA films also displayed successful patterning under a 4× objective. Patterned blue light irradiation of the 20 μM **RhBNN**−PVA-coated glass slides at 0.5 W cm^{-2} resulted in clear patterning within 10 min, which could be observed with the DLP microscope and an EVOS-*fl* microscope using an RFP filter cube (Ex = 542/20 nm and Em = 593/40, ThermoFisher, no. AMEP4952) (Figure 3D−F).

We then moved to patterning with a 40× objective for the further characterization and optimization of the visible-light microprinting chemistries. The stronger objective allowed us to focus patterns onto fields measuring 287 μm × 215 μm (2048 × 1536 px, with 1 μm = 7.14 px, as determined using ThorLabs resolution target slide no. R1L3S10P) that contained single beads as well as to achieve higher intensities of irradiation light. We projected a pattern of horizontal lines onto individual SH−resin beads in a solution of **SiR−sty** and eosin y using high intensity blue light (17.9 W cm^{-2}) through the 40× objective. Before irradiation, the beads appeared as featureless circles during fluorescence imaging, but after patterned blue light irradiation we observed horizontal lines on the beads under a uniform field of fluorescence excitation, indicating the covalent linkage of the **SiR−sty** dye at the targeted sites (Figure S6). Similarly, clear patterning was observed on the **RhBNN**−PVA-coated glass slides when they were irradiated with blue light in a horizontal lines pattern at this magnification (Figure S7). Notably, in addition to successful patterning in PVA films, the **RhBNN** Wolff rearrangement chemistry also worked for the surface functionalization of amine-labeled resin beads, displaying high precision and contrast micropatterning with blue light (Figure S7).

https://doi.org/10.1021/acscentsci.1c01234
ACS Cent. Sci. 2022, 8, 67−76

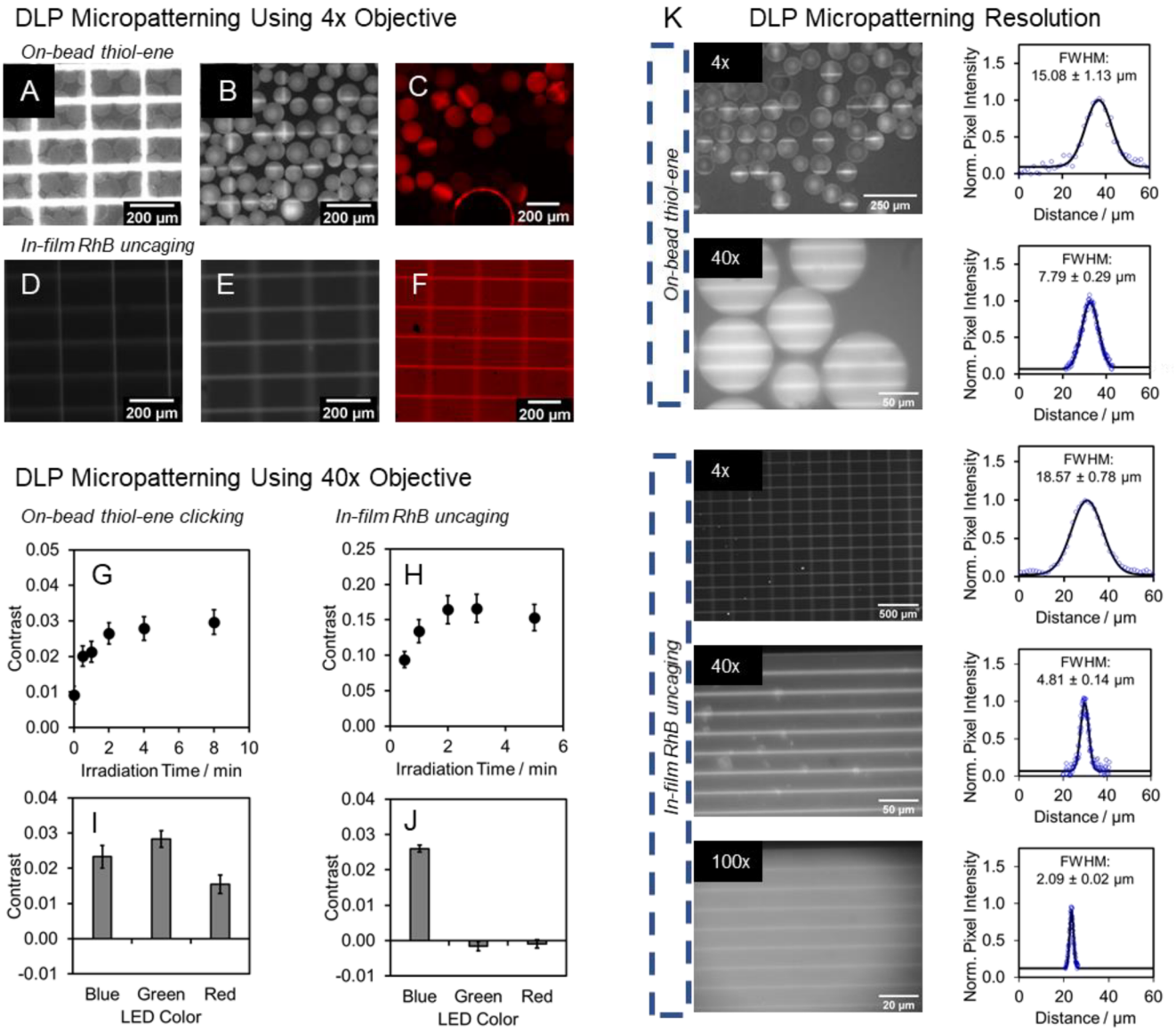

Figure 3. DLP micropatterning characterization. For DLP micropatterning with a 4× objective: fluorescence DLP microscope image of the SH−resin in **SiR−sty** (A) during irradiation with 0.5 W cm^{-2} blue light in a grid pattern for 15 min using a 4× objective and (B) after irradiation, imaged under uniform excitation through a 692/40 nm emission filter. (C) EVOS-*fl* microscope image of the resin from panel B after washing with DMSO (Ex = 635/18 nm and Em = 692/40 nm). DLP fluorescence images of the 20 μM **RhBNN**−PVA film (D) during irradiation with 0.5 W cm^{-2} blue light in a grid pattern for 10 min through a 4× objective and (E) after irradiation, imaged under uniform green light excitation through a 692/40 nm emission filter. (F) EVOS-*fl* fluorescence image of the PVA film from panel E (Ex = 542/20 nm and Em = 593/40 nm). For DLP micropatterning using a 40× objective: (G) on-resin thiol−ene patterning contrast between light and dark areas of horizontal-line-patterned beads with increasing blue light irradiation time at 17.9 W cm^{-2}. (H) **RhBNN**−PVA film patterning contrast with increasing blue light irradiation time at 17.9 W cm^{-2}. (I) Patterning contrast with varying LED colors for thiol−ene bead micropatterning after 10 min of irradiation with 8.5 W cm^{-2} blue, green, or red light. (J) Patterning contrast with varying LED colors for **RhBNN**−PVA film micropatterning after 2 min of irradiation with 8.5 W cm^{-2} blue, green, or red light. (K) Patterning resolution determination. DLP fluorescence images and representative Gaussian fits (black line) to the pixel intensity data (blue circles) for on-resin thiol−ene and in-film rhodamine B uncaging in a horizontal line or grid pattern using 4×, 40×, and 100× objectives. Errors for panels G−K are ±SE with n = 9−19 different patterned lines across 3−6 independent replicates. Images B, C, F, and K (4× objective on-bead and 40× and 100× objective in-film) are brightness- and contrast-enhanced; raw images are available in the Supporting Information.

The progress of the reactions was assessed by measuring the mean pixel intensities of SH−resin beads (Figure 3G) or **RhBNN**−PVA films (Figure 3H) at irradiated and non-irradiated areas as a measure of the contrast as it correlated with blue light irradiation times. From these experiments, the optimal irradiation times using the 40× objective with high-intensity blue light were determined to be 5 min for the thiol−ene patterning and 2 min for the rhodamine B uncaging. The contrast achieved with **RhBNN** micropatterning was substantially higher than for the thiol−ene chemistry, which may be due to the high background fluorescence emission of the **SiR−sty** solution in the thiol−ene system. In comparison, **RhBNN** is nonfluorescent prior to its reaction with the polymer

https://doi.org/10.1021/acscentsci.1c01234
ACS Cent. Sci. 2022, 8, 67−76

hydroxyl groups and thus results in high contrast upon photouncaging.

Through studies varying the irradiation light color, we found that patterning with the **RhBNN** Wolff rearrangement chemistry occurred only under blue light irradiation, while the thiol−ene micropatterning proceeded under blue, green, and red light irradiation (Figure 3I and J). Contrast data showed that blue and green light resulted in more effective thiol−ene ligation than red light did, which matches with the spectral absorbance of eosin y and provides evidence for its role as a photoinitiator in this reaction (Figure S4). Extensive control experiments allowed us to confirm that the mechanism of the **SiR−sty** patterning was indeed radical thiol−ene photoclick chemistry (Figure S6). The absence of a thiol functionality from the beads, the alkene functionality from the fluorophore, or the addition of free-radical inhibitor TEMPO led to no observed patterning. Interestingly, experiments lacking eosin y did result in some patterning, indicating that the reaction could take place without this photoinitiator, perhaps mediated by the silicon rhodamine itself,[43] though not as efficiently (Figure S6). We also studied the effect of light intensity on the patterning contrast for on-bead thiol−ene micropatterning and **RhBNN**−PVA film micropatterning and found that increasing the LED intensity generally led to higher contrast under controlled conditions, but the contrast approached a plateau at higher intensities (Figure S6 and 7).

Micropatterning Characterization. We determined the resolution of patterning with different objectives using a similar method as that used for determining the projection resolution of the DLP microscope. SH−resin beads or **RhBNN**−PVA films were irradiated with blue light in a grid pattern or a horizontal line pattern at different magnifications, and fluorescence images were then acquired under uniform excitation (Figure 3K). Intensity profiles across the patterned lines were fit to a Gaussian function, and the resolution was determined as the fwhm of the Gaussian fit in ImageJ. For the thiol−ene patterning system, on-bead patterning resolution using a 4× objective was found to be 15.08 ± 1.13 μm, and that using a 40× objective was found to be 7.79 ± 0.29 μm (Figure 3K). For the Wolff rearrangement photochemical patterning in **RhBNN**−PVA films, the resolution achieved with a 4× objective was 18.57 ± 0.78, and that achieved with a 40× objective was 4.81 ± 0.14 μm. The patterns on the PVA films were found to be persistent, and no diffusion was observed during time-lapse fluorescence microscopy of photoactivated grid patterns over 6 min at 10 s intervals (Movies S1−S3) or in fluorescence microscope images acquired 18 h after photoactivation (Figure S7C and D). Resolutions achieved on beads using the thiol−ene system with a 40× objective are lower than those on **RhBNN**−PVA films, possibly because of the curvature of the beads and the presence of a light-scattering solution surrounding the beads. Photopatterning was also achieved using a 100× objective on the **RhBNN**−PVA films with a patterning resolution of 2.09 ± 0.02 μm. For the thiol−ene on-bead patterning, although horizontal line, grid, and checkerboard patterns were observed on the beads, pixel intensities did not fit a Gaussian distribution due to low contrast between irradiated and nonirradiated areas. A conservative estimate of this patterning resolution was approximated as 3.5−5.0 μm by visual inspection of the patterned bead images (Figure S6). Combined, these results indicate that precise chemical functionalization and highly resolved micropatterning can be achieved with multicolor visible light using the DLP microscope.

Patterned Labeling of Live Cells. We next leveraged the DLP microscope and **RhBNN** Wolff rearrangement chemistry for visible-light-driven targeted labeling of live cells with fluorescent molecules. We incubated A549 lung epithelial cells grown in T25 cell culture flasks with 20 μM **RhBNN** in PBS and 2% DMSO for 30 min to allow for uptake. After rinsing with PBS, the cells were imaged on the DLP microscope and irradiated with patterned blue light at 9.4 W cm^{-2} in a split field pattern that irradiated only the left half of the field. The blue light was then removed, and the fluorescence emission of cells was imaged using a uniform field of green light at time points from 0−30 s (Figure 4A and B). As the irradiation time

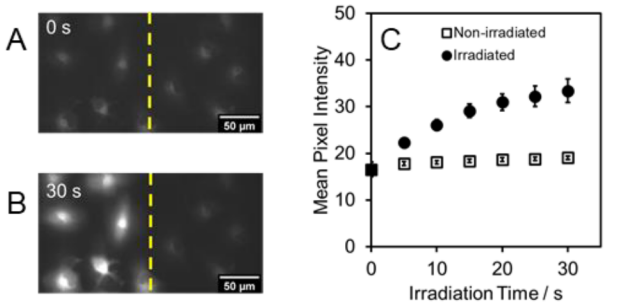

Figure 4. DLP micropatterning of live A549 cells using visible light. DLP fluorescence image of cells incubated for 30 min with 20 μM **RhBNN** under a 40× objective (A) before blue light irradiation and (B) after 30 s of blue light irradiation at 9.4 W cm^{-2} with a split field pattern, which irradiates the left half of the field. (C) Plot of average pixel intensities of all cells in the irradiated (left of the dotted line in panel B) or nonirradiated (right of the dotted line in panel B) half of the field with increasing irradiation times. Error bars are ±SD with n = 3 independent replicates. Images A and B are equally brightness- and contrast-enhanced; raw images available in the Supporting Information.

increased, cells on the irradiated left side of the field displayed increased fluorescence emission while cells on the nonirradiated right side of the field remained nonfluorescent throughout (Figure 4C), demonstrating that living cells can be targeted and selectively functionalized with fluorescent dye using visible-light-mediated chemistry and the DLP microscope.

Optimization of Procedures for Microscale Photocuring. We further explored the utility of DLP patterning by employing it for visible-light photocuring of liquid resin to achieve solid microprints, vetting it for 3D printing applications. A three-component polymerization system consisting of a dimethylacrylamide (DMA) monomer, a trimethylpropane triacrylate (TMPTA) cross-linker, and visible-light photoredox catalysts H-Nu 470, Rose Bengal, and zinc tetraphenyl porphyrin (ZnTPP) with donor and acceptor co-initiators was used.[37,38] Experiments were carried out on glass microscope slides with a 260 μm deep layer of liquid resin (Figure S8).

First, we conducted experiments to characterize the relationship between print width, light intensity, and irradiation time to optimize the micrometer-scale photocuring conditions. Vertical lines with a 74 μm width were printed from a 4:1 mixture of DMA/TMPTA, 2 wt % iodonium acceptor, 0.2 wt % borate donor, and 0.1 wt % Rose Bengal initiator with 1, 2, 3, and 4 s of irradiation time using 48, 83,

https://doi.org/10.1021/acscentsci.1c01234
ACS Cent. Sci. 2022, 8, 67−76

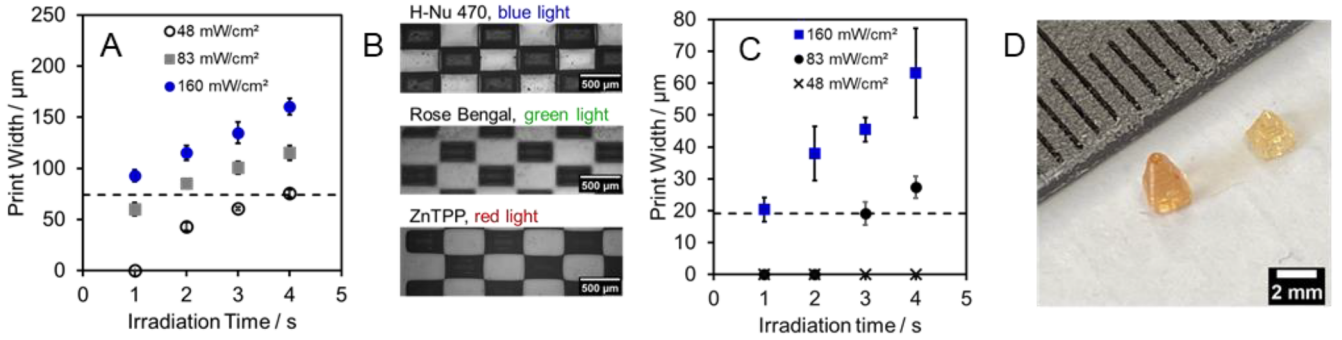

Figure 5. Optimization of DLP microscale photocuring and print resolution determination. (A) Plot of the cured print width against the irradiation time at green light irradiation intensities of 48, 83, and 160 mW cm^{-2}. The projected pattern width was 74 μm (dotted line). (B) Light microscopy images of washed prints formed on glass slides after photocuring using 83 mW cm^{-2} blue (H-Nu 470 initiator), green (Rose Bengal initiator), or red (ZnTPP initiator) irradiation light for 2 s in a checkerboard pattern. (C) Plot of the cured print width against the irradiation time at irradiation intensities of 48, 83, and 160 mW cm^{-2}. The projected pattern width was 21 μm. The dotted line represents the highest average print resolution achieved. (D) Photograph of 3D printed pyramids printed using the DLP microscope and blue-light-initiated polymer resin. Patterned light at 140 mW cm^{-2} was projected for 2 s per layer onto the bottom of a fluorinated film-lined beaker containing liquid resin, and prints were built onto a glass print bed affixed to a motorized stage for *z*-translation.

and 160 mW cm^{-2} intensities of green light through a 4× objective (Figure 5A). After washing with isopropyl alcohol, the solid prints were imaged using reflected light microscopy on the DLP microscope, and the print widths were measured in ImageJ. As the irradiation time and irradiation intensity increased, the print width was found to increase (Figure 5A). Too low or too high of an irradiation time or irradiation intensity led to prints with widths deviating from the width of the projected pattern. A close match between the print width and the projected pattern was achieved at the optimal set of photocuring conditions, which was found to be 1−2 s of irradiation at 160 or 83 mW cm^{-2}. Microprints such as the checkerboard internal test pattern of the LightCrafter system were successfully achieved with blue-, green-, and red-light-initiated photocurable resins under these conditions (Figure 5B).

Microscale Photocuring Characterization. The photocuring resolution was characterized by projecting lines of progressively smaller widths onto sample slides containing the green-light-initiated resin mixture for durations of 1−4 s at intensities of 48−160 mW cm^{-2}, with pattern widths ranging from 9.8 to 300 μm (Figure S8). The prints were washed and imaged, and widths were measured in ImageJ to determine the smallest print width that could be obtained with the micrometer-scale DLP photocuring technique. We found that prints with widths 40 μm and above could easily be achieved at all three light intensities that were studied. A finer resolution, as low as 20 μm width prints, could be attained using 80 or 163 mW cm^{-2} blue light irradiation for 3 or 1 s, respectively (Figure 5C). Attempts to improve this resolution further by reducing the projected width to 14 or 10 μm and irradiating at high intensity resulted in no print development even at long irradiation durations until time points where the printed line width surpassed 20 μm (Figure S8). This lack of intermediate print widths between zero and 20 μm suggests the limitation of a 20 μm resolution that may perhaps be overcome by the use of an inert atmosphere or oxygen scavengers.

After demonstrating the capability of the DLP microscope to photocure resin on the micrometer scale with a high resolution, we next outfitted it for 3D microprinting applications (Figure S8). The addition of a motorized stage for *z*-translation onto the existing *xy*-stage of the DLP microscope evolved it into an inverted 3D printing setup with which 3D prints such as pyramids of 1.2 mm height and 100 μm resolution in the *z*-axis were generated (Figure 5D).

Demonstrations of Microscale Chemistry. Finally, we demonstrate the versatility and ease-of-use of the DLP microscope for microprinting varied chemical functionalities and constructs (Figure 6). The top row of Figure 6 shows photocured solid 2D prints prepared from the blue-light-initiated polymerization of liquid resin on glass microscope slides using a 4× objective. Highly precise prints such as a maze pattern, a microfluidics pattern, and a printed circuit board (PCB) pattern were achieved by projecting light from a PowerPoint slide in the parallel RGB mode of LightCrafter (Figure 6A−C, respectively). Clipart and icons, including the SMU Mustang mascot and science cartoons, and text were printed on the micrometer scale with high detail and resolution (Figure 6D−F). Well-resolved 3D microprints such as the chess piece and pyramids in Figure 6G were also achieved via photopolymerization in a bottom-up 3D printing setup. The patterned surface functionalization of solid resin beads with fluorescent silicon rhodamine and rhodamine B dyes using thiol−ene chemistry and diazonium insertion chemistry is shown in the second and third rows of Figure 6. Structured light was precisely targeted on samples to achieve micropatterning on individual beads using a 40× objective in shapes, text, and patterns such as the yin-yang symbol, a checkerboard pattern, and a star, among others (Figure 6H−M). The two chemistries could also be carried out orthogonally on SH− resin beads, with prolonged red or green light irradiation mediating the thiol−ene photoclicking with **SiR−sty** and quick flashes of patterned blue light uncaging and trapping **RhBNN** on beads. Fluorescence emission in distinct patterns from the distinct fluorophores was individually imaged through the appropriate emission filters (Figure 6N). Live cells were easily labeled with rhodamine B using diazoketone Wolff rearrangement chemistry; highly confluent fields of cells were labeled in a split field pattern and a checkerboard pattern under a 4× objective (Figure 6O and P), and desired individual cells could be targeted for single-cell activation using a 40× objective (Figure 6Q). Detailed photographs, which maintained their contrast and resolution over prolonged periods, were printed onto PVA films using the photo-uncaging of **RhBNN**. A

https://doi.org/10.1021/acscentsci.1c01234
ACS Cent. Sci. 2022, 8, 67−76

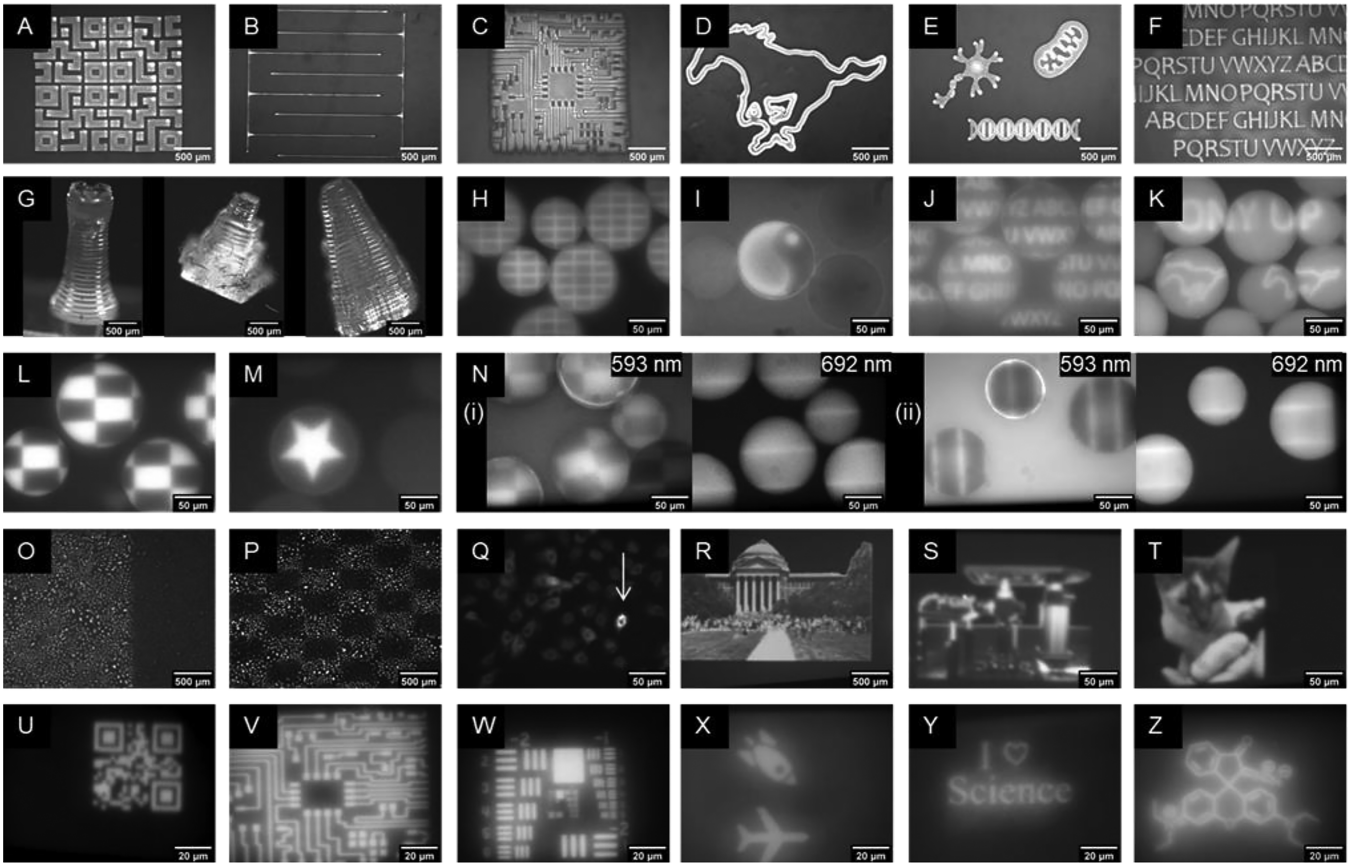

Figure 6. Demonstration of DLP microscale photocuring, 3D printing, on-bead micropatterning, live-cell labeling, and film patterning. Fluorescence DLP images of microscale photocured solid resin showing (A) a maze pattern; (B) a microfluidics pattern; (C) a printed circuit board pattern; (D) the SMU mustang mascot; (E) neuron, mitochondria, and DNA clipart; and (F) alphabet text. (G) Fluorescence images of a DLP 3D microprinted rook and pyramids. Thiol−ene patterning of **SiR-Sty** on SH−resin beads in (H) a grid pattern, (I) a yin-yang pattern, (J) alphabet text, and (K) the SMU mustang mascot and "PONY UP" slogan. Rhodamine B modification of NH_2-resin beads in (L) a checkerboard pattern and (M) a star pattern. (N) Dual patterning of **RhBNN** (fluorescence imaged through a 593/20 nm filter) and **SiR−sty** (fluorescence imaged through a 692/40 nm filter) on SH−resin beads in (i) a checkerboard and horizontal line pattern and (ii) a pattern of vertical and horizontal lines. Fluorescence images of live A549 cells labeled with rhodamine B in (O) a split field pattern, (P) a checkerboard pattern, and (O) a desired single cell labeled in a confluent field of cells. Fluorescence DLP images of microprinting in **RhBNN**−PVA films showing (R) the Dallas Hall building, (S) the DLP microscope, (T) a pet cat, (U) a QR code, (V) a printed circuit board pattern, (W) the United States Air Force resolution test pattern, (X) rocket and airplane clipart, (Y) "I heart Science" text, and (Z) the structure of rhodamine BNN. Scale bars correspond to the magnifying objective used for patterning and imaging; the scale bar represents 500 μm with a 4× objective, 50 μm with a 40× objective, and 20 μm with 100× objective. Images I, J, N−R, and T− W are brightness- and contrast-enhanced; raw images are available in the SI.

photograph of the Dallas Hall building was printed on a 2.5 mm × 1.7 mm area of film (1840 × 1268 px, with 1 μm = 0.73 px) using the 4× objective (Figure 6R). Photographs of the DLP microscope and a closeup of a cat were printed with a 40× objective (Figure 6S and T) on areas as small as 170 μm × 210 μm (1246 × 1506 px, 1 μm = 7.14 px). Intricate patterning was also achieved under a 100× objective on the **RhBNN**−PVA film, including a functional QR code measuring 48 μm × 48 μm (850 × 850 px, with 1 μm = 17.8 px) that breaks the current world record,[44] a printed circuit board pattern with feature sizes of 2 μm, resolution charts, and legible text, icons, and chemical structures that were generated with only seconds of light irradiation and no required wash steps (Figure 6U−Z). These demonstrations showcase the range of applications and chemical versatility of DLP chemical micropatterning.

CONCLUSIONS

In summary, we present a visible-light-based chemical micropatterning technique comprised of a home-built digital light processing (DLP) fluorescence microscope and photochemical reaction systems. The DLP microscope is capable of spatially structuring blue, green, and red visible light for the targeted excitation and photoinitiation of micrometer-scale samples via focusing lenses, reaching projection resolutions finer than half a micron. Interchangeable light filters and a CMOS camera enable fluorescence imaging and light microscopy in this modular system. We optimized and leveraged visible-light-based thiol−ene photoclicking and diazoketone Wolff rearrangements for the real-time-observable printing of silicon rhodamine and rhodamine B molecules onto solid resin beads with resolutions better than 10 μm using red, green, and blue light. Microprints approaching a 2 μm resolution were achieved through the photo-uncaging of **RhBNN** in PVA films with structured blue light without the need for washing steps, providing stunning examples of photograph-quality microscopic prints and the world's smallest QR code to date. DLP micropatterning was also employed in the targeted fluorescent labeling of selected single live cells from confluent fields. The resin photocuring ability of the DLP

https://doi.org/10.1021/acscentsci.1c01234
ACS Cent. Sci. 2022, 8, 67−76

microscope and stereolithography 3D printing applications were also examined, and we showed that solid 2D polymer prints with a 20 μm *xy*-resolution and 3D prints with a 100 μm *z*-resolution could be generated without specialty equipment.

Owing to the versatility and ease-of-use of DLP chemical microprinting, we envision a wide range of ground-breaking applications for this technique that span across fields such as 3D printing, nanorobotics, and metamaterials. Compatibility with living cells offers potentially transformative technology to target molecules to specific cells and subcellular structures such as cell nuclei, filopodia, or even single synapses with a high level of control and throughput. To manifest these possibilities and unlock doors to more emerging areas, we continue to explore advanced optical setups and chemistry that will elevate the resolution, contrast, throughput, and chemical compatibility of visible-light DLP chemical microprinting to new heights.

■ ASSOCIATED CONTENT

Supporting Information

The Supporting Information is available free of charge at https://pubs.acs.org/doi/10.1021/acscentsci.1c01234.

Experimental details, supplementary images, and scanned spectra (PDF)

Time-lapse fluorescent microscopy video of photoactivated grid patterns (AVI)

Time-lapse fluorescent microscopy video of photoactivated grid patterns (AVI)

Time-lapse fluorescent microscopy video of photoactivated grid patterns (AVI)

■ AUTHOR INFORMATION

Corresponding Author

Alexander R. Lippert − *Department of Chemistry, Southern Methodist University, Dallas, Texas 75205-0314, United States; Center for Drug Discovery, Design, and Delivery (CD4), Southern Methodist University, Dallas, Texas 7205-0314, United States;* orcid.org/0000-0003-4396-0848; Email: alippert@smu.edu

Authors

Uroob Haris − *Department of Chemistry, Southern Methodist University, Dallas, Texas 75205-0314, United States*

Joshua T. Plank − *Department of Chemistry, Southern Methodist University, Dallas, Texas 75205-0314, United States*

Bo Li − *Department of Chemistry, Southern Methodist University, Dallas, Texas 75205-0314, United States*

Zachariah A. Page − *Department of Chemistry, The University of Texas at Austin, Austin, Texas 78712, United States;* orcid.org/0000-0002-1013-5422

Complete contact information is available at: https://pubs.acs.org/10.1021/acscentsci.1c01234

Author Contributions

U.H. was responsible for conceptualization, methodology, investigation, visualization, writing the original draft, reviewing, and editing. J.T.P. was responsible for conceptualization, methodology, investigation, visualization, reviewing, and editing. B.L. was responsible for resources and investigation. Z.A.P. was responsible for resources, reviewing, editing, and conceptualization. A.R.L. was responsible for conceptualization, methodology, investigation, visualization, writing the original draft, reviewing, editing, supervision, project administration, and funding acquisition. All authors have given approval to the final version of the manuscript.

Notes

The authors declare the following competing financial interest(s): A.R.L. discloses a financial stake in BioLum Sciences, LLC.

■ ACKNOWLEDGMENTS

We acknowledge funding from the American Chemical Society Petroleum Research Fund (60759-ND1) and the Welch Foundation (N-2038-20200401 for A.R.L. and F-2007 for Z.A.P.).

■ ABBREVIATIONS

DLP, digital light processing; DMD, digital micromirror device; NA, numerical aperture; Fmoc, fluorenylmethyloxycarbonyl; fwhm, full-width at half-maximum; Mmt, monomethoxytrityl; PVA, poly(vinyl alcohol)

■ REFERENCES

(1) Liddle, J. A.; Gallatin, G. M. Nanomanufacturing: A Perspective. *ACS Nano* **2016**, *10* (3), 2995−3014.

(2) Li, J.; Pumera, M. 3D printing of functional microrobots. *Chem. Soc. Rev.* **2021**, *50* (4), 2794−2838.

(3) Lee, M.; Rizzo, R.; Surman, F.; Zenobi-Wong, M. Guiding Lights: Tissue Bioprinting Using Photoactivated Materials. *Chem. Rev.* **2020**, *120* (19), 10950−11027.

(4) Wang, L.; Pumera, M. Recent advances of 3D printing in analytical chemistry: Focus on microfluidic, separation, and extraction devices. *TrAC, Trends Anal. Chem.* **2021**, *135*, 116151.

(5) Hüll, K.; Morstein, J.; Trauner, D. In Vivo Photopharmacology. *Chem. Rev.* **2018**, *118* (21), 10710−10747.

(6) Velema, W. A.; Szymanski, W.; Feringa, B. L. Photopharmacology: Beyond Proof of Principle. *J. Am. Chem. Soc.* **2014**, *136* (6), 2178−2191.

(7) Mao, M.; He, J.; Li, X.; Zhang, B.; Lei, Q.; Liu, Y.; Li, D. The Emerging Frontiers and Applications of High-Resolution 3D Printing. *Micromachines* **2017**, *8* (4), 113.

(8) Altissimo, M. E-beam lithography for micro-/nanofabrication. *Biomicrofluidics* **2010**, *4*, 026503.

(9) Kim, C. S.; Ahn, S. H.; Jang, D. Y. Review: Developments in micro/nanoscale fabrication by focused ion beams. *Vacuum* **2012**, *86* (8), 1014−1035.

(10) Liu, G.; Petrosko, S. H.; Zheng, Z.; Mirkin, C. A. Evolution of Dip-Pen Nanolithography (DPN): From Molecular Patterning to Materials Discovery. *Chem. Rev.* **2020**, *120* (13), 6009−6047.

(11) Sreenivasan, S. V. Nanoscale Manufacturing Enabled by Imprint Lithography. *MRS Bull.* **2008**, *33* (9), 854−863.

(12) Fairbanks, B. D.; Macdougall, L. J.; Mavila, S.; Sinha, J.; Kirkpatrick, B. E.; Anseth, K. S.; Bowman, C. N. Photoclick Chemistry: A Bright Idea. *Chem. Rev.* **2021**, *121* (12), 6915−6990.

(13) Li, L.; Lin, Q.; Tang, M.; Tsai, E. H. R.; Ke, C. An Integrated Design of a Polypseudorotaxane-Based Sea Cucumber Mimic. *Angew. Chem., Int. Ed.* **2021**, *60* (18), 10186−10193.

(14) Jin, K.; Tian, Y.; Erickson, J. S.; Puthoff, J.; Autumn, K.; Pesika, N. S. Design and Fabrication of Gecko-Inspired Adhesives. *Langmuir* **2012**, *28* (13), 5737−5742.

(15) Valentine, J.; Li, J.; Zentgraf, T.; Bartal, G.; Zhang, X. An optical cloak made of dielectrics. *Nat. Mater.* **2009**, *8*, 568−571.

(16) Zheng, X.; Smith, W.; Jackson, J.; Moran, B.; Cui, H.; Chen, D.; Ye, J.; Fang, N.; Rodriguez, N.; Weisgraber, T.; Spadaccini, C. M. Multiscale metallic metamaterials. *Nat. Mater.* **2016**, *15*, 1100−1106.

(17) *TI DLP LightCrafter 4500 Evaluation Module User's Guide*; Texas Instruments Incorporated: Dallas, Texas, 2017. https://www.ti.com/lit/ug/dlpu011f/dlpu011f.pdf (accessed on 2021-05-18).
(18) Sun, C.; Fang, N.; Wu, D. M.; Zhang, X. Projection micro-stereolithography using digital micro-mirror dynamic mask. *Sens. Actuators, A* **2005**, *121* (1), 113−120.
(19) Zhu, W.; Li, J.; Leong, Y. J.; Rozen, I.; Qu, X.; Dong, R.; Wu, Z.; Gao, W.; Chung, P. H.; Wang, J.; Chen, S. 3D-Printed Artificial Microfish. *Adv. Mater.* **2015**, *27* (30), 4411−4417.
(20) Kang, M.; Han, C.; Jeon, H. Submicrometer-scale pattern generation via maskless digital photolithography. *Optica* **2020**, *7* (12), 1788−1795.
(21) Dinh, D. H.; Chien, H. L.; Lee, Y. C. Maskless lithography based on digital micromirror device (DMD) and double sided microlens and spatial filter array. *Opt. Laser Technol.* **2019**, *113*, 407−415.
(22) Lee, M. P.; Cooper, G. J. T.; Hinkley, T.; Gibson, G. M.; Padgett, M. J.; Cronin, L. Development of a 3D printer using scanning projection stereolithography. *Sci. Rep.* **2015**, *5*, 9875.
(23) Durand-Silva, A.; Cortés-Guzmán, K. P.; Johnson, R. M.; Perera, S. D.; Diwakara, S. D.; Smaldone, R. A. Balancing Self-Healing and Shape Stability in Dynamic Covalent Photoresins for Stereolithography 3D Printing. *ACS Macro Lett.* **2021**, *10* (4), 486−491.
(24) Oliver, C. R.; Gourgou, E.; Bazopoulou, D.; Chronis, N.; Hart, A. J. On-Demand Isolation and Manipulation of C. elegans by In Vitro Maskless Photopatterning. *PLoS One* **2016**, *11* (1), No. e0145935.
(25) Dorsey, P. J.; Rubanov, M.; Wang, W.; Schulman, R. Digital Maskless Photolithographic Patterning of DNA-Functionalized Poly(ethylene glycol) Diacrylate Hydrogels with Visible Light Enabling Photodirected Release of Oligonucleotides. *ACS Macro Lett.* **2019**, *8* (9), 1133−1140.
(26) Li, D.; Miao, A.; Jin, X.; Shang, X.; Liang, H.; Yang, R. An automated 3D visible light stereolithography platform for hydrogel-based micron-sized structures. *AIP Adv.* **2019**, *9*, 065204.
(27) Lu, P.; Ahn, D.; Delafresnaye, L.; Yunis, R.; Corrigan, N.; Boyer, C.; Barner-Kowollik, C.; Page, Z. A. Wavelength-selective light-matter interactions in polymer science. *Matter* **2021**, *4* (7), 2172−2229.
(28) Hoyle, C. E.; Bowman, C. N. Thiol-Ene Click Chemistry. *Angew. Chem., Int. Ed.* **2010**, *49* (9), 1540−1573.
(29) Lowe, A. B. Thiol-ene "click" reactions and recent applications in polymer and materials synthesis: a first update. *Polym. Chem.* **2014**, *5*, 4820−4870.
(30) Shih, H.; Lin, C. C. Visible-Light-Mediated Thiol-Ene Hydrogelation Using Eosin-Y as the Only Photoinitiator. *Macromol. Rapid Commun.* **2013**, *34* (3), 269−273.
(31) DeForest, C. A.; Anseth, K. S. Cytocompatible Click-based Hydrogels with Dynamically-Tunable Properties Through Orthogonal Photoconjugation and Photocleavage Reactions. *Nat. Chem.* **2011**, *3*, 925−931.
(32) Dobos, A.; Van Hoorick, J.; Steiger, W.; Gruber, P.; Markovic, M.; Andriotis, O. G.; Rohatschek, A.; Dubruel, P.; Thurner, P. J.; Van Vlierberghe, S.; Baudis, S.; Ovsianikov, A. Thiol-Gelatin-Norbornene Bioink for Laser-Based High-Definition Bioprinting. *Adv. Healthcare Mater.* **2020**, *9* (15), 1900752.
(33) Belov, V. N.; Wurm, C. A.; Boyarskiy, V. P.; Jakobs, S.; Hell, S. W. Rhodamines NN: A Novel Class of Caged Fluorescent Dyes. *Angew. Chem., Int. Ed.* **2010**, *49* (20), 3520−3523.
(34) Thiel, Z.; Rivera-Fuentes, P. Single-Molecule Imaging of Active Mitochondrial Nitroreductases Using a Photo-Crosslinking Fluorescent Sensor. *Angew. Chem., Int. Ed.* **2019**, *58*, 11474−11478.
(35) Ciszewski, Ł. W.; Rybicka-Jasińska, K.; Gryko, D. Recent developments in photochemical reactions of diazo compounds. *Org. Biomol. Chem.* **2019**, *17*, 432−448.
(36) Hu, J.; Liu, Y.; Khemtong, C.; El Khoury, J. M.; McAfoos, T. J.; Taschner, I. S. Photochemical Patterning of a Self-Assembled Monolayer of 7-Diazomethylcarbonyl-2,4,9-trithiaadmantane on Gold Films via Wolff Rearrangement. *Langmuir* **2004**, *20* (12), 4933−4938.
(37) Ahn, D.; Stevens, L. M.; Zhou, K.; Page, Z. A. Rapid High-Resolution Visible Light 3D Printing. *ACS Cent. Sci.* **2020**, *6* (9), 1555−1563.
(38) Stafford, A.; Ahn, D.; Raulerson, E. K.; Chung, K.; Sun, K.; Cadena, D. M.; Forrister, E. M.; Yost, S. R.; Roberts, S. T.; Page, Z. A. Catalyst Halogenation Enables Rapid and Efficient Polymerizations with Visible to Far-Red Light. *J. Am. Chem. Soc.* **2020**, *142* (34), 14733−14742.
(39) Patel, S. K.; Cao, J.; Lippert, A. R. A Volumetric Three-Dimensional Digital Light Photoactivatable Dye Display. *Nat. Commun.* **2017**, *8*, 15239.
(40) Li, B.; Haris, U.; Aljowni, M.; Nakatsuka, A.; Patel, S. K.; Lippert, A. R. Tuning the Photophysical Properties of Spirolactam Rhodamine Photoswitches. *Isr. J. Chem.* **2021**, *61*, 244.
(41) Ryan, L. S.; Gerberich, J.; Haris, U.; Nguyen, D.; Mason, R. P.; Lippert, A. R. Ratiometric pH Imaging Using a 1,2-Dioxetane Chemiluminescence Resonance Energy Transfer Sensor in Live Animals. *ACS Sens.* **2020**, *5*, 2925−2932.
(42) Butkevich, A. N.; Bossi, M. L.; Lukinavičius, G.; Hell, S. W. Triarylmethane Fluorophores Resistant to Oxidative Photobluing. *J. Am. Chem. Soc.* **2019**, *141* (2), 981−989.
(43) Wang, C.; Zhang, H.; Zhang, T.; Zou, X.; Wang, H.; Rosenberger, J. E.; Vannam, R.; Trout, W. S.; Grimm, J. B.; Lavis, L. D.; Thorpe, C.; Jia, X.; Li, Z.; Fox, J. M. Enabling *In Vivo* Photocatalytic Activation of Rapid Bioorthogonal Chemistry by Repurposing Silicon-Rhodamine Fluorophores as Cytocompatible Far-Red Photocatalysts. *J. Am. Chem. Soc.* **2021**, *143* (28), 10793−10803.
(44) Smallest QR Code. *Guiness World Records*. https://www.guinnessworldrecords.com/world-records/626800-smallest-qr-code (accessed on 2021-10-04).

https://doi.org/10.1021/acscentsci.1c01234
ACS Cent. Sci. 2022, 8, 67−76